Preprint Title	Gold nanoparticle-decorated reduced graphene oxide (rGO) as a highly reactive catalyst for the selective α,β-dehydrogenation of N-methyl-4-piperidone
Authors	Brenda Flore Kenyim, Mihir Tzalis, Marilyn Kaul, Robert Oestreich, Aysenur Limon, Chancellin Pecheu Nkepdep and Christoph Janiak
Publication Date	17 Jul 2025
Article Type	Full Research Paper
Supporting Information File 1	SI pip-fin.docx; 1.4 MB
ORCID® iDs	Mihir Tzalis - https://orcid.org/0009-0005-0527-6318; Chancellin Pecheu Nkepdep - https://orcid.org/0009-0009-4004-2057; Christoph Janiak - https://orcid.org/0000-0002-6288-9605

Gold nanoparticle-decorated reduced graphene oxide (rGO) as a highly reactive catalyst for the selective α,β-dehydrogenation of N-methyl-4-piperidone

Brenda Flore Kenyim[1], Mihir Tzalis[1], Marilyn Kaul[1], Robert Oestreich[1], Aysenur Limon[1], Chancellin Pecheu Nkepdep[1], Christoph Janiak[1]*

[1] Institut für Anorganische Chemie und Strukturchemie, Heinrich-Heine-Universität, 40204 Düsseldorf, Germany.

Christoph Janiak - janiak@uni-duesseldorf.de (C.J.)

* Corresponding author

Abstract

Gold nanoparticles (AuNPs) supported on reduced graphene oxide (AuNPs/rGO) were demonstrated to be a highly reactive catalyst for the selective α, β-oxidative dehydrogenation (ODH) of N-methyl-4-piperidone as a model substrate for β-N-substituted saturated ketones. This substrate was chosen due to the significant pharmaceutical relevance of the reaction product 1-methyl-2,3-dihydropyridin-4(1H)-one which is very expensive (>1000 €/g), in contrast to the inexpensive starting material (0.15 €/g). Various synthesis methods were employed to prepare AuNPs supported on different carbon materials, including reduced graphene oxide (rGO), activated carbon (AC), and carbon black (CB), to investigate the influence of the carbon support on the catalyst performance. As stabilizing agents for the AuNPs citrate (Cit) and the polyoxometallate $[SiW_9O_{34}]^{10-}$ (SiW_9) were used. Among the tested catalysts, the rGO-supported ones, Au-Cit/rGO, Au-SiW_9/rGO, Au@SiW_9/rGO and exhibited superior catalytic activity for the selective oxidation reaction. These findings offer valuable insights for the design of highly active Au-based catalysts for the dehydrogenation of β-N-substituted saturated ketones and other fine chemical applications.

Keywords

Supported gold nanoparticles; Oxidative dehydrogenation; Reduced graphene oxide; β-N-substituted ketones.

Introduction

The high-surface area properties of matter at the nanometric scale have led to many catalytic studies at the industrial and laboratory scale [1]. Nanocatalysis is no longer just an academic field, but a rapidly evolving field for industries wishing to develop green and sustainable processes with very high turnover numbers, turnover rates and stabilities [2].

The development of highly efficient catalysts is of constant interest for advancements in organic chemistry, particularly in oxidation, hydrogenation, and coupling reactions. Gold nanoparticles (AuNPs) have emerged as exceptionally effective catalysts for facilitating these types of reactions [3,4]. The unique catalytic properties of AuNPs stem from their nanoscale size, which increases the surface-to-volume ratio, exposes a higher density of active sites, and induces quantum size effects that modulate the electronic structure [5]. These characteristics collectively enhance their reactivity, selectivity, and tunability, making AuNPs highly versatile in catalytic applications [5,6]. Traditional ligands such as thiols and citrates are commonly used in the synthesis of AuNPs due to their ability to control particle size, prevent aggregation, and enhance stability in solution [7]. Also, polyoxometalates (POMs) have emerged as stabilizing ligands for nanoparticles offering distinct structural and electronic advantages. They are widely utilized in various catalytic processes, including oxidation, acid-base, and photocatalysis [8,9] POMs have been extensively employed for stabilizing and decorating small metal nanoparticles, including gold nanoparticles [10,11]. POMs can act as both reducing and capping agents [12]. Recently in 2022, Xia et al. demonstrated that among the fully occupied ($[SiW_{12}O_{40}]^{4-}$, SiW_{12}), monovacant ($[SiW_{11}O_{39}]^{8-}$, SiW_{11}), divacant ($[SiW_{10}O_{36}]^{8-}$, SiW_{10}), and trivacant ($[SiW_9O_{34}]^{10-}$, SiW_9) silicotungstate POMs, the latter trivacant species exhibits the highest Au-POM reactivity in the oxidative dehydrogenation of piperidone derivatives to the corresponding enaminones [13]. Through the oxygen atoms at its three vacant sites, SiW_9 coordinates to gold metal atoms, forming strong interactions. Despite being coated with strong ligands that provide initial stability over time, ligand desorption, ligand exchange, or environmental factors such as pH and ionic strength can weaken the protective layer, leading to nanoparticle aggregation or structural degradation [14,15].

An important aspect of expensive noble-metal nanoparticles in heterogeneous catalysis is their separation from the reaction mixture for re-use, recycling and also to avoid contamination of the products. The difficulty in separating small nanoparticles demands for the efficient and easy formation of a composite which can be separated by filtration and where the NPs are further stabilized against coalescence, aggregation, sintering or Ostwald ripening under the catalytic reaction conditions. By anchoring AuNPs onto a solid support, such as metal oxides, polymers, or carbon-based materials, their stability is significantly enhanced, preventing unwanted coalescence and preserving their functional properties over extended periods [16].

Carbon-based materials such as activated carbon (AC) [17], reduced graphene oxide (rGO) and carbon black (CB) have gained considerable attention as supports due to their resistance to acid and basic environments, their tunable surface area and surface chemistry and electrical conductivity [18,19]. To deposit metal NPs onto a carbon support, procedures such as adsorption or reduction-deposition (RD), co-precipitation**,** impregnation, and deposition precipitation (DP) are commonly employed [6,19].

Carbon supported gold nanoparticles (Au/C) have been extensively studied for their remarkable selective catalytic performance in low-temperature oxidation reactions, including CO oxidation, alcohol oxidation, hydrocarbon oxidation, amino and thiol oxidation, and glucose oxidation [20]. However, despite their widespread use in direct oxidation processes, Au/C have been less explored in selective α,β-oxidative dehydrogenation reactions, particularly for β-N-substituted saturated ketones [19,21].

In this study, gold nanoparticles with an average size of 10–15 nm, stabilized by sodium citrate (NaCit), and of 3-8 nm, stabilized by SiW_9 and supported on the three-carbon materials AC, rGO and CB by the RD and DP methods were synthesized as depicted in Figure 1. To assess the differences in the preparation and of the carbon supports, the catalytic activity was tested with the model reaction of the oxidative dehydrogenation of N-methyl-4-piperidone to 1-methyl-2,3-dihydropyridin-4(1H)-one. The relevance of this reaction lies in the fact that the product is a valuable intermediate in medicinal chemistry. Its derivatives have demonstrated significant biological activities, including anti-cancer and anti-bacterial effects [22]. The pharmaceutical relevance of this compound is further underscored by its high market value (>1000 €/g), in stark contrast to the low cost of the starting material.

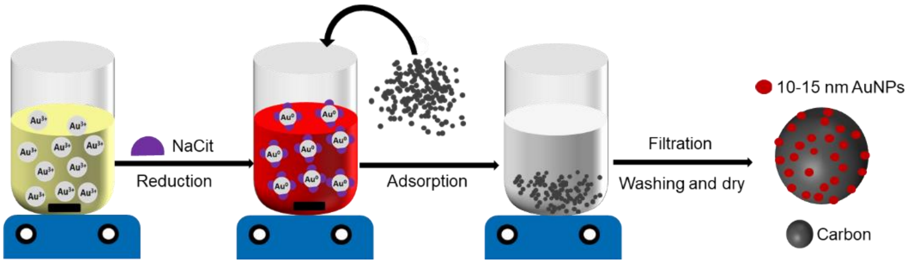

(a) Reduction-deposition (RD) with NaCit.

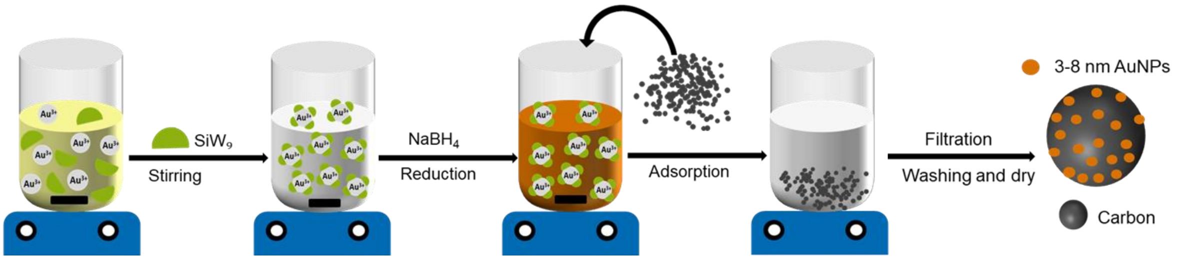

(b) Reduction-deposition (RD) with SiW$_9$

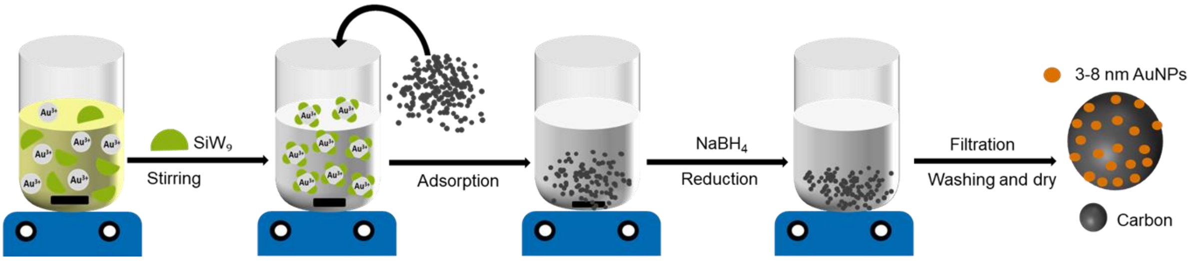

(c) Deposition-precipitation (DP) with SiW$_9$

Figure 1: Schematic representation of the carbon-supported gold catalyst preparation through the reduction-deposition method with a) sodium citrate, b) with SiW$_9$ and c) the deposition-precipitation method with SiW$_9$. In each method the three different carbon materials activated carbon (AC), reduced graphene oxide (rGO) and carbon black (CB) were used. "Au^{3+}" refers to the tetrachloridoaurate (III) anion $[AuCl_4]^-$ in the KAuCl$_4$ starting material.

Results and Discussion

Description and characterization of the carbon support (AC, rGO, CB)

The morphological and textural properties of the carbon supports are critical for their performance as catalysts in AuNP-supported systems. To assess these properties, scanning electron microscopy (SEM) and nitrogen gas sorption surface area analysis using the Brunauer-Emmett-Teller (BET) theory were employed to evaluate the surface structure, porosity, and overall texture of the materials.

The SEM image in Figure 2a reveals the typical structure of AC, characterized by a heterogeneous, rough surface with lamellar layers and pronounced macroporosity. The rGO carbon (Figure 2b) exhibits a structure composed of thin, wrinkled, and sheet-like layers, characteristic of exfoliated graphene-based materials. The morphology of CB (Figure 2c) is formed of highly aggregated small particles.

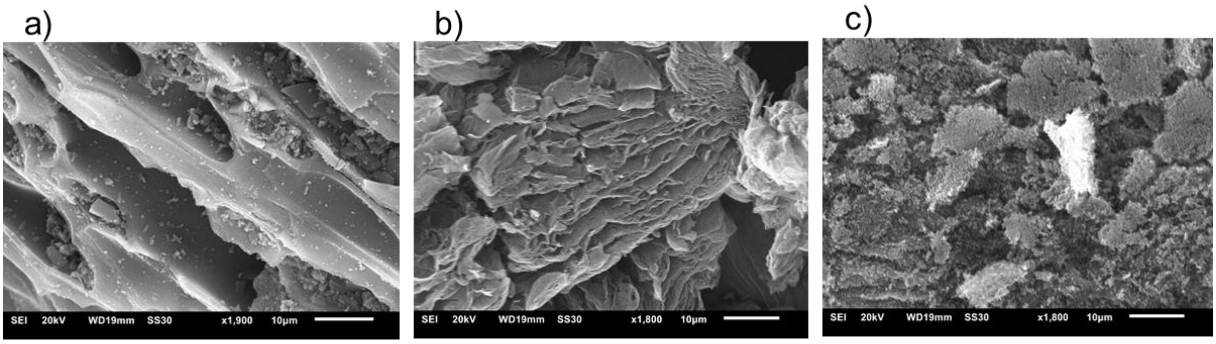

Figure 2: SEM images (10 µm scale) of a) AC, b) rGO, and c) CB.

The nitrogen sorption isotherms and their hysteresis loops in Figure 3 supplement the SEM analysis of the three carbon materials in terms of specific BET surface area, pore volume and size. AC features a reversible almost Type I isotherm, given by microporous materials with narrow micropores around 1 nm, with a small Type II contribution at larger P/P_0 and a small H4 hysteresis loop which is given by the mesoporous part of AC. rGO has a Type II isotherm due to unrestricted monolayer-multilayer adsorption up to high P/P_0 and where the multilayer appears to increase without limit when P/P_0 reaches 1. The wide H3 hysteresis loop is typically given by non-rigid aggregates of platelets as seen in rGO (cf. Figure 2b). CB also gives a combination of a Type I and Type II isotherm, albeit with an overall small uptake and a very narrow H3 hysteresis loop. The lower limit of this H3 loop is located at the cavitation-induced P/P_0 which is at a high value of 0.9 in CB vs. 0.45 in rGO [23].

Among the three carbon materials activated carbon exhibited the highest BET surface area (751 m^2/g) and intermediate total pore volume (0.81 cm^3/g). Its pore diameters are largely below 2 nm and indicate a predominantly microporous structure, which may limit mass transport and hinder catalytic performance in reactions requiring easy access to active sites. Reduced graphene oxide has a moderate BET surface area (231 m^2/g), but the highest total pore volume (2.03 cm^3/g). The pore diameters extend into the mesoporous region (2-50 nm) for a large fraction of the pores (Figure 4b). This combination suggests a more open and accessible porous network, facilitating better mass transport and diffusion of reactants and products to and from the active sites. Carbon black shows the lowest BET surface area (167 m^2/g) and total pore volume (0.57 cm^3/g). Most of the pores are again in the microporous region (< 2 nm) (Figure 4c), concomitant with a less accessible structure, which could limit catalytic performance.

Although activated carbon has the highest surface area, its low microporous nature (Figure 4a) may limit accessibility to active sites. In contrast, rGO presents a balanced combination of a reasonably high surface area, a larger pore diameter, and the highest pore volume. These features provide a more favourable environment for mass transport, reactant diffusion, and nanoparticle dispersion, making rGO a more effective catalyst support, so we expect a better catalytic activity with the gold supported rGO.

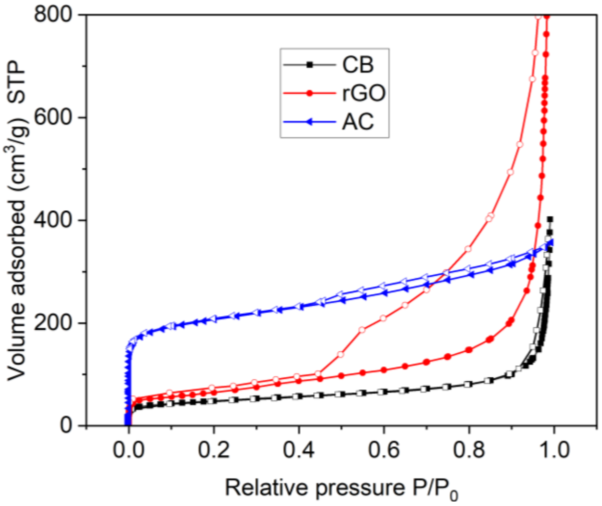

Figure 3: Nitrogen sorption isotherms of the three carbon materials at 77 K (filled symbols adsorption, empty symbols desorption).

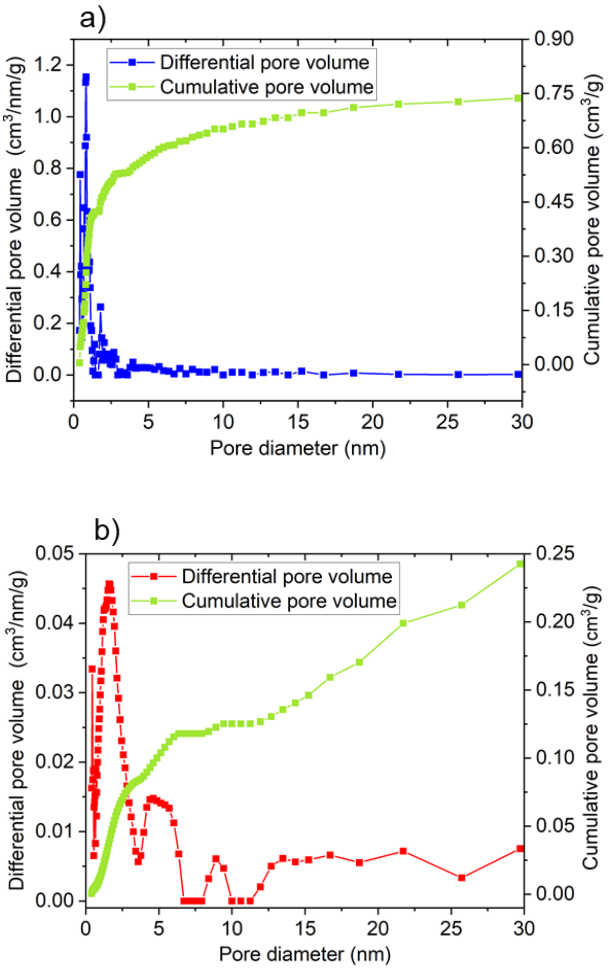

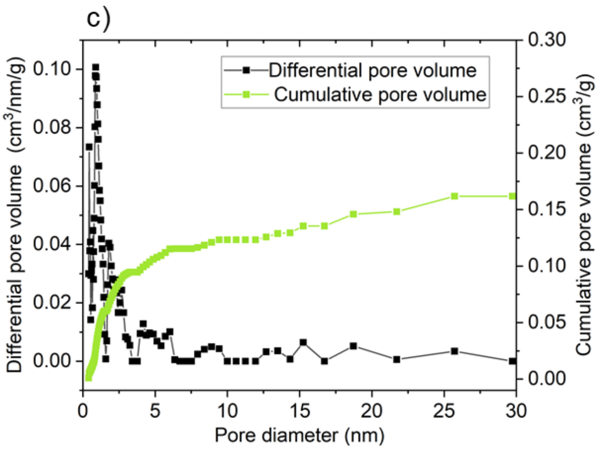

Figure 4. Pore size distributions curves a) AC, b) rGO, c) CB

In addition to the morphological and textural properties of carbon supports, which have an impact on the dispersion of metal nanoparticles and the overall efficiency of the catalytic process, the presence and distribution of functional groups is also a crucial factor in the choice of carbon support. Several studies have demonstrated that the amount of surface oxygen-containing functional groups strongly influences catalytic activity [24,25]. AC contains a significant number of functional groups, such as carboxyls, hydroxyls, and phenols, which enhance its interaction with metal nanoparticles and improve catalytic performance [26,27], rGO possesses a higher amount of oxygen functional groups than AC [27]. In contrast, CB has fewer oxygen-containing functional groups, making it more chemically inert with weaker metal-support interactions [28]. Based on these findings [27,28], the abundance of oxygen-containing functional groups among the studied carbon supports follows the order rGO > AC > CB, making rGO probably the most active and efficient support for NPs.

Synthesis and characterization of carbon supported gold nanoparticles

The synthesis of the Au-Cit/carbon and of the Au-SiW_9/carbon composities was carried out by the reduction-deposition (RD) method as schematically depicted in Figure 1a, b. This method involved the synthesis of AuNPs in a colloidal solution, using sodium citrate both as a reducing and stabilizing agent (Figure 1a) or the silicotungstate polyoxometallate SiW_9 as a stabilizer with $NaBH_4$ as the reducing agent (Figure 1b). The preformed nanoparticles are then deposited onto the carbon material. The synthesis of the Au@SiW_9/carbon composites was done by the deposition-precipitation (DP) method as shown in Figure 1c where the POM salt (SiW_9), the gold precursor ($KAuCl_4$) and the carbon material are combined in a solution-dispersion and then reduction is induced with $NaBH_4$.

Synthesis of citrate-coated AuNPs on carbon (Au-Cit/AC, Au-Cit/rGO, and Au-Cit/CB)

The citrate-coated AuNPs (Au-Cit) were synthesized by the Turkevich method, one of the most widely used bottom-up techniques. In this process, the gold salt $KAuCl_4$ is reduced by sodium citrate (NaCit) when the aqueous solution is heated to boiling. Upon adding sodium citrate to the tetrachloridoaurate(III) solution, the solution initially becomes decolorized as gold(III) is reduced to gold(I). After a few minutes, the solution turns violet, signalling the formation of AuNPs, which then transition to a ruby red color as the AuNPs disperse. This result is a gold nanoparticle colloidal suspension.

The presence of AuNPs was confirmed by the appearance of a localized surface plasmon resonance (LSPR) band in the visible wavelength range, with a maximum absorbance at λ_{max} = 519 nm (Figure 5a). The hydrodynamic radius (HD) by numberweighted distribution of dynamic light scattering (DLS) measurements was approximately 12 nm (Figure 5b). Transmission electron microscopy (TEM) analysis showed spherical and well-dispersed nanoparticles and their particle size distribution (Figure 5c), based on the measurements of 200 nanoparticles, yielded an average diameter of 12 nm with a standard deviation of ±1 nm (Figure 5d), which agrees with the size obtained by DLS.

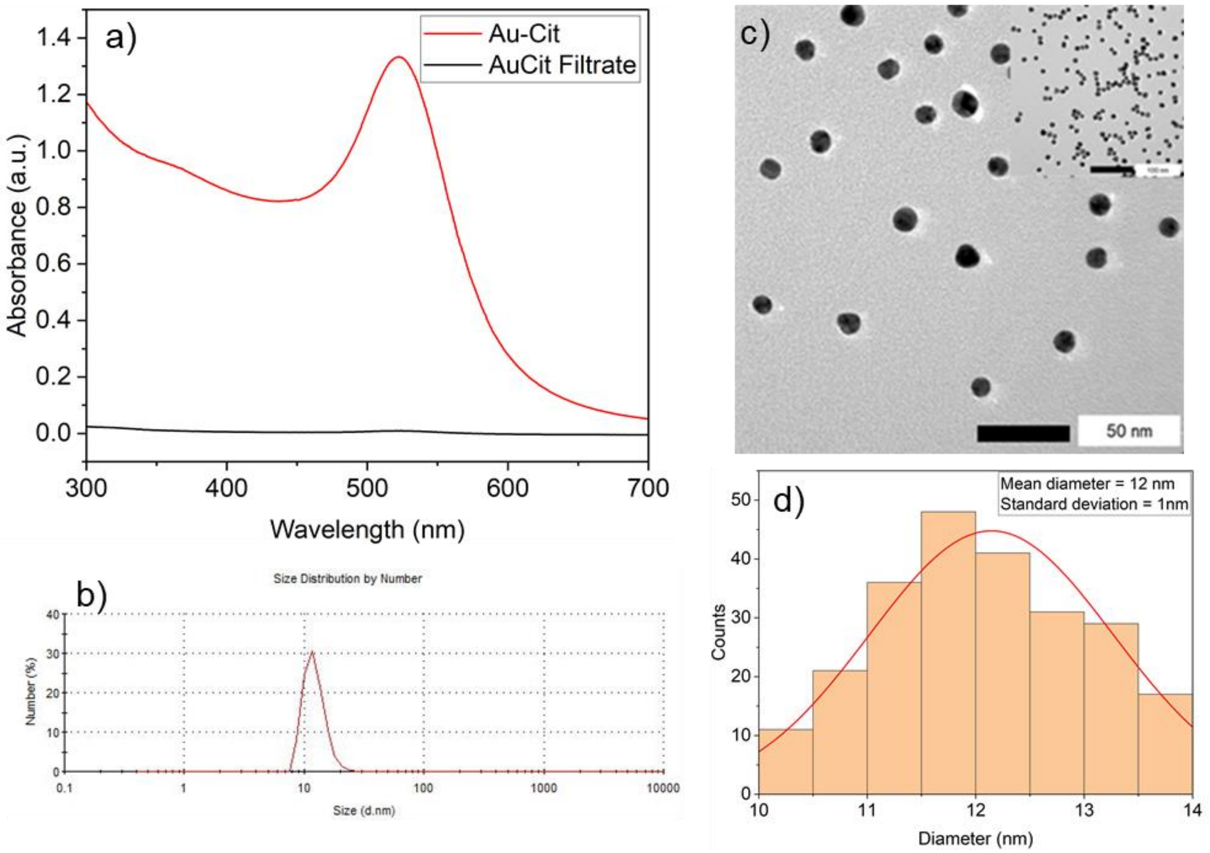

Figure 5: a) Localized surface plasmon resonance absorption band of AuNPs present in the dispersion (Au-Cit) and the spectrum of the filtrate after AuNP deposition on carbon; b) DLS of Au-Cit. c) TEM images of Au-Cit and its histogram particle size distributions. Conditions: n_{KAuCl_4} = 53 µmol, n_{NaCit} = 319 µmol, temperature = 100 °C.

Immediately after synthesizing three batches of the citrate-coated AuNPs, the three different carbon materials AC, rGO, and CB were individually introduced into each batch. In all cases, this resulted in complete discoloration of the dispersion to a clear solution with a black precipitate (Figure 1a), indicating the successful deposition of AuNPs onto the carbon supports. This was further confirmed by spectrophotometric analysis of the filtrate, which showed the disappearance of the LSPR band (Figure 5a). Subsequently, the successful AuNP deposition on the carbon materials was validated through TEM imaging of Au-Cit/AC (Figure 6a), Au-Cit/rGO (Figure 6b), and Au-Cit/CB (Figure 6c). Upon deposition the average AuNP particle sizes had slightly grown to 13 nm within a range of 10-16 nm determined by TEM images and the corresponding histogram distributions. After immobilisation on carbon, the supported AuNPs show all a similar average size and size distribution but slightly larger than that of the unsupported Au colloids (11 nm). This growth was probably due to continuous agitation during colloid immobilisation.

Noteworthy, the AuNPs are evenly distributed on rGO but occupy only certain areas on AC and especially on CB, thereby leaving large section on the CB surface without AuNPs. This is in agreement with the fewer oxygen-containing functional groups leading to less metal-support interactions on CB [15].

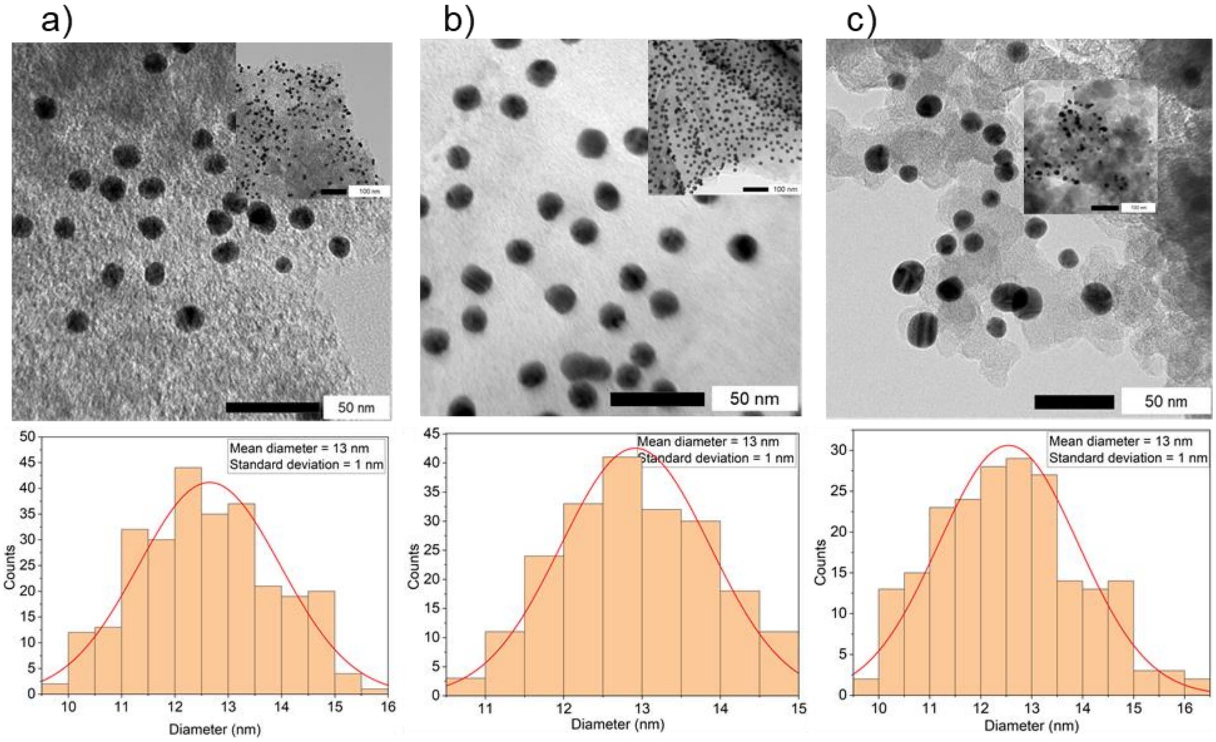

Figure 6: TEM images of a) Au-Cit/AC, b) Au-Cit/rGO, c) Au-Cit/CB with the inserts showing a wider area and their corresponding histogram particle size distributions below each of them.

Synthesis of SiW_9-coated AuNPs on carbon (Au-SiW_9/AC, Au-SiW_9/rGO, and Au-SiW_9/CB)

Unlike the synthesis of Au-Cit, which takes place under hot conditions, the synthesis of Au-SiW_9 is performed in the cold at 2 °C to prevent the isomerization of the POM. First, the sodium salt of SiW_9 ($Na_{10}SiW_9O_{34}$) was synthesized following a well-established protocol [29] and characterized by powder X-ray diffraction (PXRD) (see SI). An ice-cold solution of sodium borohydride ($NaBH_4$) was added dropwise to an aqueous solution containing $KAuCl_4$ and the sodium salt of SiW_9, resulting in the formation of an orange-brown dispersion (Figure 1b). UV-Vis. spectroscopy revealed the characteristic LSPR band at 508 nm, confirming the presence of gold nanoparticles (Figure 7a). Compared to Au-Cit with λ_{max} = 519 nm, the blue shift observed toward a shorter wavelength for Au-SiW_9 indicated the formation of smaller nanoparticles, which was further confirmed by DLS analysis, showing an average particle diameter of approximately 4 nm (Figure 7b).

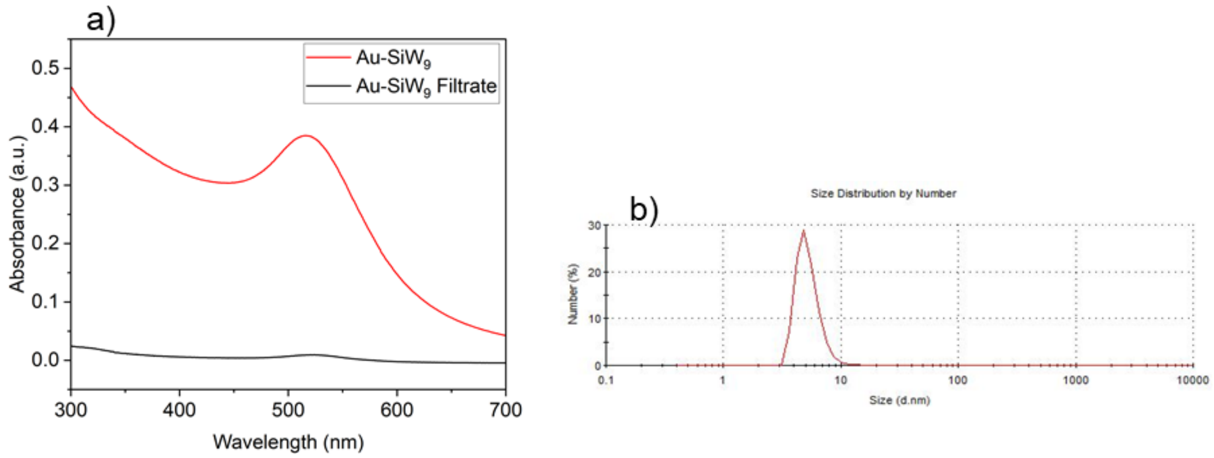

Figure 7: a) Plasmon resonance absorption band of AuNPs present in the dispersion (Au-SiW_9) and the spectra of the filtrate after AuNPs deposition on AC, rGO and CB; b) DLS of Au-SiW_9 dispersion. Conditions: n_{KAuCl_4} = 15 µmol, n_{SiW_9} = 15 µmol, n_{NaBH4} = 150 µmol, temperature = 2 °C.

Following the formation of the colloidal suspension of Au-SiW_9, the carbon supports (AC, rGO and CB) were added. This addition resulted in a slight discoloration of the dispersion, transitioning from brown-orange to colorless within a few minutes. This change indicates the successful deposition of Au-SiW_9 onto the carbon supports. The successful deposition was further confirmed through UV-vis analysis of the filtrate obtained after the filtration step, which revealed the disappearance of the characteristic LSPR band at 508 nm (Figure 7a). The TEM images of the synthesized composites, , Au-SiW_9/rGO (Figure 8a) and Au-SiW_9/CB (Figure 8b), revealed small, spherical, and well-dispersed particles. The particle size was between 2-8 nm with an average of 5-6 nm and a standard deviation of ±1 nm, as determined from their corresponding histogram distributions (Figure 8). The Au-SiW$_9$/AC composite had already been synthesized by Xia et al. [13] and our results of particle size and distribution closely match their outcomes, confirming the successful deposition and comparable dispersion of gold nanoparticles on the activated carbon support.

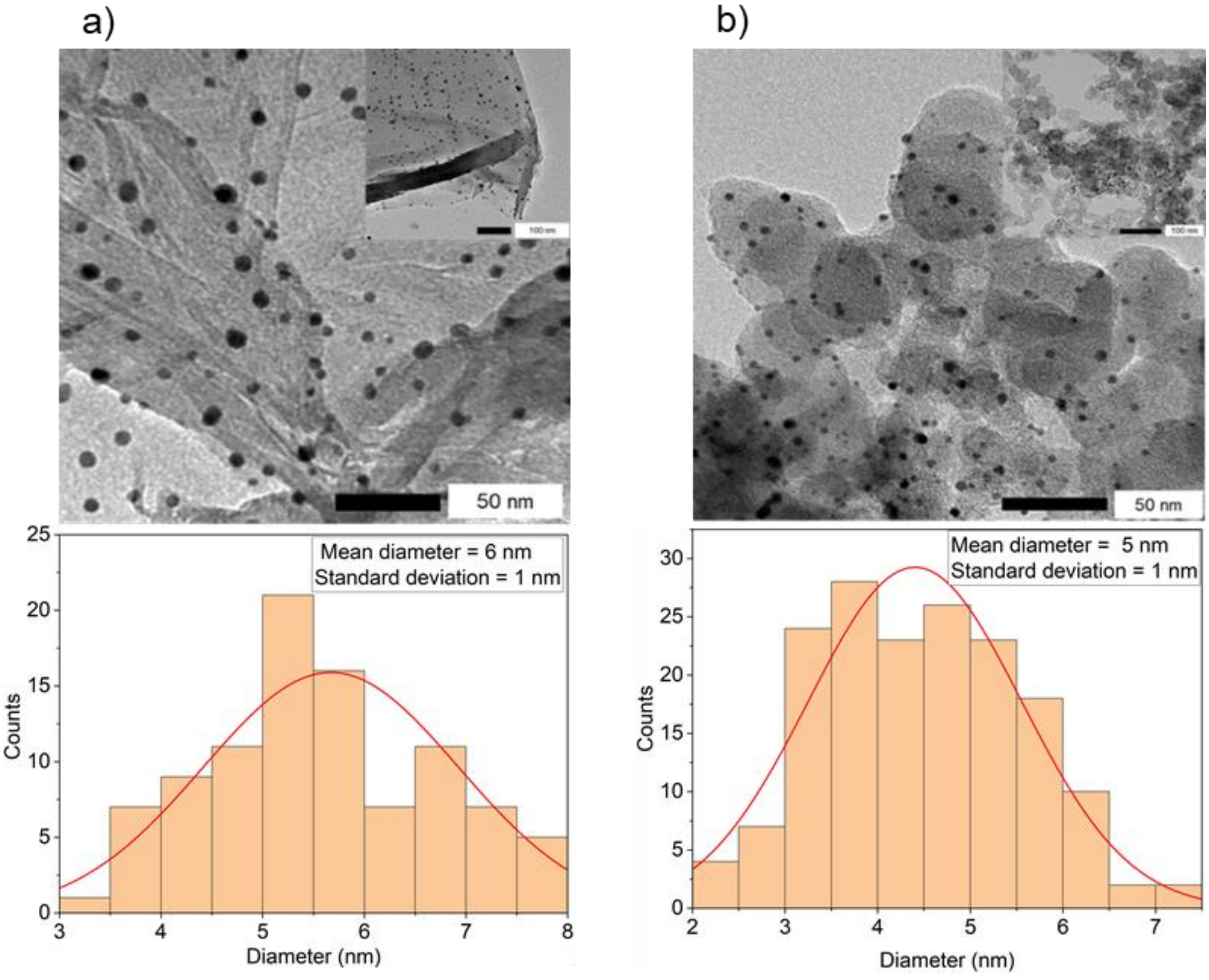

Figure 8: TEM images of a) Au-SiW$_9$/AC, b) Au-SiW$_9$/rGO and c) Au-SiW$_9$/CB with the inserts showing a wider area and their corresponding histogram particle size distributions.

Synthesis of Au@SiW_9/AC, Au@SiW_9/rGO and Au@SiW_9/CB.

The deposition-precipitation (DP) method is the most widely used procedure to support gold nanoparticles on metal oxides [6]. The synthesis involves dissolving the POM salt (SiW_9) and the gold precursor ($KAuCl_4$) in water in an ice bath, dispersing the carbon material (AC, rGO, CB) in the solution, allowing the POM salt and gold precursor to adsorb onto the carbon surface or in the pores, and then reduction with $NaBH_4$ is induced to form Au@SiW_9/AC, Au@SiW_9/rGO, Au@SiW_9/CB. Unlike the RD method, where the reduction of the tetrachloridoaurate(III) ions to metallic gold occurs in solution and is observable through a color change before the addition of the carbon material, the DP synthesis method induces the reduction within the pores or on the surface of the carbon black support (Figure 1c). As a result, no color change is perceptible when the amount of carbon was sufficient to capture the gold precursor from solution. Hence, also no DLS analysis on the AuNPs will be possible. Only TEM analysis can be used to characterize the gold nanoparticles within the carbon matrix.

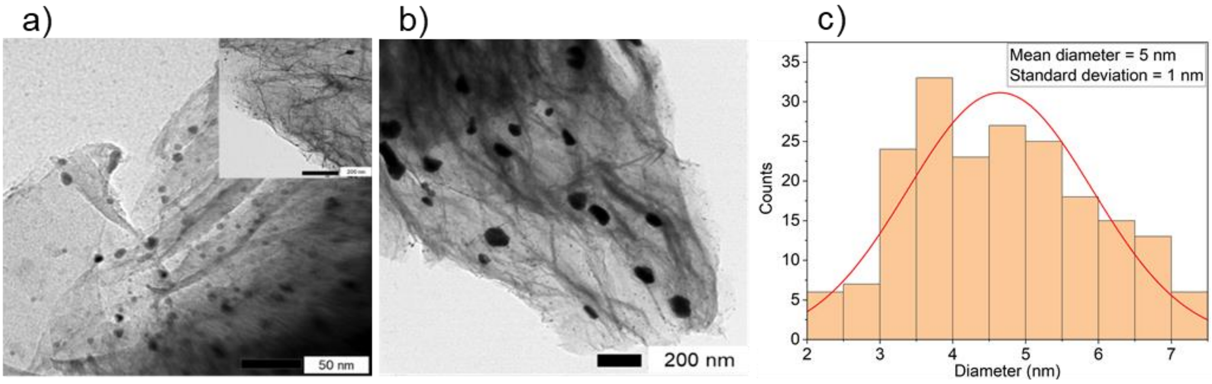

Figure 9: TEM images of Au@SiW_9/rGO at two different magnifications and the corresponding histogram particle size distribution.

Upon examining the TEM images at 50 nm magnification of the Au@SiW_9/rGO system synthesized via DP (Figure 9a), it is evident that the AuNPs are less dense and less discernible than from the RD method (cf. Figure 8a). The average particle size is 5 nm in a range between 2-7 nm, as determined from their corresponding histogram distributions. There are also strongly aggregated AuNPs seen in many sections of the Au@SiW_9/rGO composite (Figure 9b). For Au@SiW_9/AC and Au@SiW_9/CB such strong aggregation is all what is seen for the Au@SiW_9 particles (Figure S2). According to the literature it is indeed aggregates and no individual large particles [6,30]. These observations suggests that, during the adsorptive pre-deposition process, the anionic $[AuCl_4]^-$ precursor will adsorb at different regions or smaller pores than the larger SiW_9 anions intended for stabilization. When the reduction is induced there will not be enough POM anions in the vicinity to prevent aggregation. Uneven precursor distribution can lead to localized high concentrations of Au species, resulting in less controlled nucleation and the formation of larger clusters. Surface roughness and heterogeneity of the support influence the size and distribution, leading to increased aggregation of AuNPs [31,32]. Evidently, rGO with its higher amount of mesopores and functional oxygen groups is the only carbon material among the three which still allows for the formation of a significant fraction of non-aggregated AuNPs.

The PXRDs of the AuNPs deposited on rGO carbon by the different methods show the crystallinity of the AuNPs, with the four distinct diffraction peaks at 38.4° (111), 44.5° (200), 64.8° (220), and 77.8° (311), which correspond to the characteristic diffraction pattern of the face-centered cubic (fcc) gold lattice [33]. The first distinct diffraction peak at $2\theta = 25.5°$ is attributed to the (100) reflection of rGO [34].

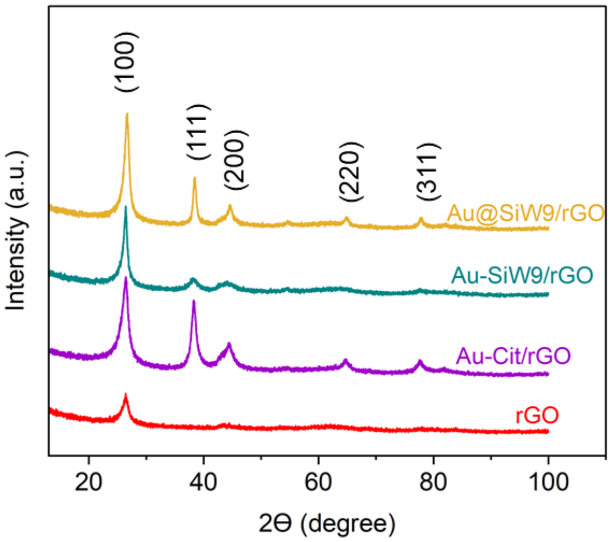

Figure 10: PXRD pattern of crystalline gold nanoparticles deposited on rGO.

The crystallite size of the gold nanoparticles (AuNPs) is determined by X-ray diffraction (XRD) analysis using the Scherrer equation below. In this context, the shape factor K, often referred to as the Scherrer constant, is influenced by several factors, including the crystallite's shape, degree of size uniformity, and the nature of the diffraction peak. For nanoparticles with a spherical shape and cubic symmetry, a commonly adopted value for K is 0.94 [35]. D represents the average crystallite size, λ is the X-ray wavelength (0.1542 nm), β corresponds to the full width at half maximum (FWHM) of the diffraction peak (in radians), and θ is the Bragg angle, which is half of the 2θ value. The average crystallite dimension was found to be approximately 14 nm for the catalyst Au-Cit/rGO and 7 nm for Au-SiW_9/rGO and Au@SiW_9/rGO.

$$D = \frac{k\ \lambda}{\beta\ \cos(\theta)}$$

The average crystallite size was determined to be approximately 15 nm for the Au-Cit/rGO catalyst, and around 7 nm for both Au-SiW9/rGO and Au@SiW9/rGO. These values correlate with the particle size distributions observed in the TEM histogram analysis. The slight variation in measured sizes can be attributed to limitations of the instrumentation, the presence of structural defects, the complexity of signal-sample interactions, and background noise [36]. As a result, it can be challenging to distinguish peak broadening caused specifically by crystallite size from that induced by other contributing factors [37,38]. Nevertheless, the Scherrer equation remains a valuable tool for estimating the average size of nanoparticles based on X-ray diffraction data.

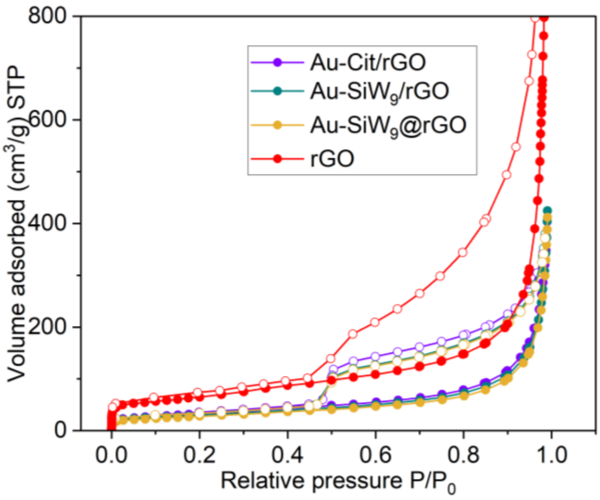

Figure 11: Nitrogen sorption isotherms of the AuNP/rGO composites at 77 K (filled symbols adsorption, empty symbols desorption).

After the deposition of AuNPs, the BET surface area and total pore volume of the composites showed significantly lower values compared to the neat rGO. This reduction suggests that AuNPs partially occupy the porous network of rGO with pore blocking, thereby limiting the accessible surface area.

Catalytic test of the carbon supported AuNPs

To evaluate the efficiency of the synthesized AuNP-carbon composites, we selected the relevant oxidative dehydrogenation of 1-methyl-4-piperidone to 1-methyl-2,3-dihydropyridin-4(1H)-one as a model reaction (Scheme 1). This transformation is an example for the synthesis of β-N-substituted α,β-unsaturated ketones and requires catalysts with strong oxidizing capabilities, such as gold-based catalysts.

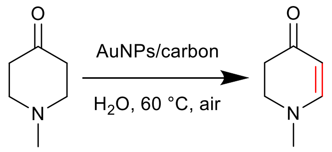

Scheme 1: α,β-oxidative dehydrogenation of N-methyl-4-piperidone to 1-methyl-2,3-dihydropyridin-4(1H)-one with gold catalysts and aerial oxygen in aqueous dispersions.

The nine carbon-supported gold nanoparticle materials synthesized in this study were evaluated under identical conditions (Table 2), focusing on conversion, selectivity and yields. Blank tests demonstrated that the neat carbon supports (AC, rGO, CB) without gold loading exhibited no catalytic activity. Conversion rates and yields of the reaction were determined by gas chromatography (GC) using calibration curves of the starting material and the product (see SI).

The amount of supported gold in the composite was calculated by assuming quantitative conversion of the gold precursor to the nanoparticles as well as quantitative uptake of the AuNPs (cf. Figure 5a and 7a) onto the carbon support material. The progress of the reaction was followed by GC for the rGO catalyst composites (Figure 12a) so that the reaction was stopped when 100% conversion was reached after 6 or 7 h for the most active systems. Also, for the less active, usually CB-based catalysts the reaction was then stopped after 8 h and the conversion and yield were determined.

Table 2: Catalytic results in the selective ODH of 1-methyl-4-piperidone to 1-methyl-2,3-dihydropyridin-4(1H)-one.[a]

Entry	Catalyst	Au (wt%) [b]	Catalyst (mg) [c]	Au (mol%) [d]	Time (h)	Conversion (%) [e]	Yield (%) [f]
1	Au-Cit/AC	1.04	100	2.12	8	100	90
2	Au-Cit/rGO	10.44	10	2.12	7	100	98
3	Au-Cit/CB	2.08	50	2.12	8	60	48
4	Au-SiW_9/AC	0.42	100	0.85	8	100	88
5	Au-SiW_9/rGO	4.22	10	0.85	6	100	98
6	Au-SiW_9/CB	0.84	50	0.85	8	42	22
7	Au@SiW_9/AC	0.42	100	0.85	8	85	62
8	Au@SiW_9/rGO	4.22	10	0.85	7	100	98
9	Au@SiW_9/CB	0.84	50	0.85	8	23	11

[a] Reaction conditions: 30 mg, 0.25 mmol of 1-methyl-4-piperidone, 2 mL of water, open air 1.013 bar, temperature 60°C.

[b] Weight fraction of Au in the composite, calculated by assuming quantitative uptake of the AuNPs or the gold precursor onto the carbon material.

[c] Amount of applied composite in the catalysis. The amount was chosen so as to achieve the same molar fraction of Au in the reaction mixture of the three Au-X/carbon catalysts.

[d] Molar ratio of gold to starting material (× 100%) in the reaction mixture: mol% Au = (mol Au / mol piperidone) × 100%.

[e] Conversion was determined from the molar concentration of the starting material before the reaction minus the starting material after the reaction divided by the concentration of the starting material before (× 100%). The concentration was derived from the GC signal area (Figure S5) with the calibration curves (Figure S4a).

[f] Yield was determined from the molar amount of the product divided by the used molar amount of the starting material (× 100%). The molar amount of the product was determined from the GC signal area (Figure S5) with the calibration curve (Figure S4b).

All catalysts are 100% selective in the formation of 1-methyl-4-piperidone to 1-methyl-2,3-dihydropyridin-4(1H)-one; there are no side products. In the cases of less than 100% conversion, unreacted starting material accounted for the difference. Yields of less than 100% were due to the adsorption of product in the pores of the carbon materials.

As we can clearly observe in Table 2, catalysts with carbon black (CB) as support showed lower conversion and yields while AuNPs supported on AC and rGO achieved complete or near complete conversion of the reactant over time. However, AC was somewhat less effective compared to rGO-as support because of a longer reaction time needed to achieve quantitative conversion (8 vs 7 or 6 h). This may be attributed to the surface chemistry and largely microporous structure of activated carbon, which hinders efficient mass transport and diffusion of reactants. In the case of Au@SiW_9-AC a conversion of only 85% was reached after 8 h while the rGO analogue gave 100%. In contrast, the textural and morphological properties of rGO, characterized by enhanced mesoporosity, provide a more favourable environment for catalyst dispersion and improved reaction kinetics. This is attributed to the high oxygen content of rGO, which enables efficient anchoring of AuNPs, resulting in higher catalytic efficiency.

In addition, the AC-based composites tend to retain the product within their microporous structure even after multiple washings, resulting in a lower yield of the desired product compared to the rGO composites, despite the same 100% conversion. In contrast, all catalysts supported on rGO (Entries 2, 5, and 8, Table 2) consistently exhibited a high yield of 98%. This enhanced performance can be attributed to the structural characteristics of rGO, which facilitate more efficient mass transfer and enabled complete release of the product after the reaction and subsequent washing steps. Compared to AC and CB, the lamellar structure and lower microporosity of rGO minimize product entrapment, thereby enhancing overall catalytic efficiency. These textural properties make rGO the most effective support for AuNP catalysts.

However, a very important point to consider when using carbon supports in catalysis is the gold loading in the support. Compared to AC and CB, rGO exhibits a lower bulk density due to its high porosity and than the other carbon materials AC and CB, as illustrated in Figure S3 (see SI). When comparing the two reduction methods, hot reduction with NaCit and cold reduction with POM (SiW_9), important differences arise in nanoparticle formation. NaCit is a mild reducing agent that reduces Au^{3+} slowly, leading to gradual nucleation. As a result, fewer gold nuclei form, and each nucleus has time to grow into a larger particle. In contrast, $NaBH_4$ is a strong reducing agent that rapidly reduces Au^{3+} under cold conditions, triggering a burst of nucleation, this produces many small gold nuclei almost instantly, leaving little precursor available for further growth. The outcome is a high number of small AuNPs with greater surface area and a higher number of catalytically active sites. Beyond the improved stability of AuNP-based POMs — attributable to the steric bulk of the POMs — this fundamental difference in synthesis also helps to explain why the Au-SiW_9/AC and Au-SiW_9/rGO catalyst, despite having more than two times lower gold loading than the Au-Cit/AC and Au-Cit/rGO catalyst (Entry 4-5 vs. 1-2, Table 2), still exhibits comparable catalytic activity.

The Au-SiW$_9$/AC catalyst, originally synthesized by Xia et al. [13], was reproduced in this study with a key difference of gold loading. Xia et al. used 3.17 wt% Au, corresponding to 2.5 mol% Au in the oxidation reaction. In this study, we used only 0.42 wt% Au in the composite and 0.85 mol% in the catalysis, yet achieved better conversion and higher yield for the same target reaction. Xia et al. reported a conversion of 92% and a yield of 86% as their best result. This clearly highlights that catalytic activity of gold is not solely dependent on the amount of gold, but rather on the dispersion of gold nanoparticles, which increases the number of accessible active sites and reduces the need for excessive gold loading. In fact, increasing gold content can be detrimental, as it may lead to particle aggregation, thereby reducing the surface area and number of active sites. Thus, the superior performance of the low-loaded Au-SiW$_9$/AC catalyst synthesized in this study compared to the higher-loaded Au-SiW$_9$/C catalyst reported by Xia et al. demonstrates the critical role of nanoparticle dispersion and size control in achieving efficient catalytic performance.

For the AC- and CB-based composites a higher catalytic activity of nanoparticles synthesized by RD (Entry 1-6) compared to those formed by DP (Entry 7-9, Table 2) can be attributed to the AuNP dispersion and aggregation**.** In RD synthesis, preformed AuNPs are adsorbed onto the carbon surface in a controlled manner, ensuring uniform dispersion (Figure 6 and 8) and consequently maximal exposure to reactants. This enhances catalytic efficiency by providing greater access to active sites. Conversely, the DP synthesis results usually in less uniform particles due to uncontrolled nucleation and growth, which reduces the active surface area. Moreover, AuNPs became partially embedded within the carbon matrix, reducing their access and availability for catalytic reactions [39]. Consequently, the composites prepared by RD typically exhibit superior catalytic performance compared to their DP-derived counterparts.

To enable a meaningful comparison of the catalysts' activity over time, TON and TOF values were analyzed after each hour from one to six hours (Figure 12a, 12b, Table S.7). The catalytic performance over time underscores a long-term stability of Au-SiW_9/rGO. It not only achieved the highest TON (118) but also maintained a steady increase in TON and only a slow decrease in TOF after two hours among the three catalysts, reflecting its ability to continuously convert substrate over time with minimal deactivation. In contrast, Au-Cit/rGO, despite its initially high activity, experienced a significant decline, with TOF dropping to 18 h^{-1} and TON reaching 108, indicating a notable reduction in catalytic efficiency, despite the much higher gold loading (Table 2). Au@SiW_9/rGO exhibited the lowest values at 6 hours (TON = 106, TOF = 18 h^{-1}), confirming its comparatively lower overall catalytic performance. This trend reinforces the earlier observation that Au-Cit/rGO is more effective for short reaction times, whereas Au-SiW_9/rGO proves to be the most robust and efficient for prolonged catalytic processes.

The catalyst Au@SiW_9 also appears to be suitable for long-term reactions. Although it exhibits a slower reaction rate due to the preparation method as discussed earlier, it maintains a more consistent catalytic activity over time than Au-Cit/rGO.

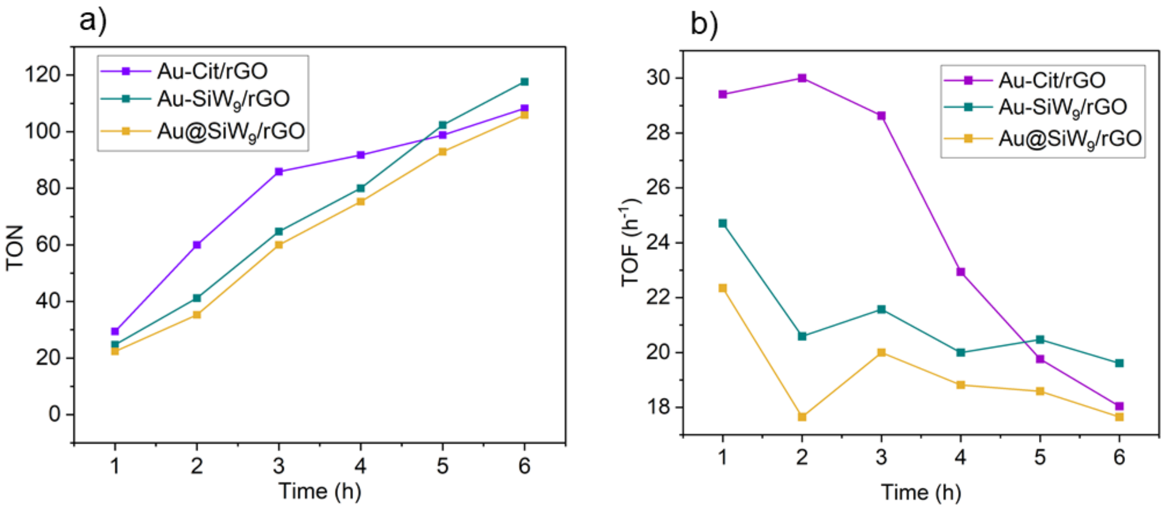

Figure 12: a) TON and TOF of the rGO based catalyst at each hour of the reaction (see Table S6 for the data).

An important aspect in the AuNPs heterogenization on a carbon support is the separation, recycling and reuse of the catalyst which also concerns the stability of the catalyst. This was tested for the most active rGO-based catalysts over four runs. The catalysts were separated by filtration using standard filter paper, then thoroughly washed and dried before being reused in subsequent reaction cycles. In fact, catalytic stability tests after four reactions cycles (Figure 13) show that for or the Au-Cit catalyst the conversion within the fixed time of 7 h dropped from 100% to 89% which was more than for the Au-SiW$_9$ catalysts (6 h), which dropped from 100% to only 94%. The Au-Cit and Au-SiW$_9$ catalysts were prepared by the reduction deposition (RD) method. The Au@SiW$_9$/rGO catalyst which was obtained by the deposition-precipitation (DP) method retains its full catalytic activity with 100% conversion in 7 h even after 4 cycles (Figure 13). These results highlight the effectiveness of the POM SiW$_9$ in stabilizing the nanoparticles, thereby preserving their catalytic activity over recycling and extended use.

Thus, the AuNPs on rGO synthesized by the RD method, appear to be less stable and become less catalytically active over time than those formed via DP. This may be due to the metal-support interaction in RD, where the citrate or SiW_9 POM coated AuNPs adhere to rGO mainly through electrostatic forces rather than direct AuNP-rGO chemical bonding. As a result, these nanoparticles are more susceptible to detachment, and aggregation over time, especially under catalytic conditions. In contrast, DP leads to in situ nucleation and growth of AuNPs directly on the rGO surface, with the possibility of forming direct metal–oxygen bonds to rGO that enhance particle anchoring. Therefore, while RD-synthesized AuNPs may offer better dispersion and catalytic accessibility, they are inherently less stable compared to those formed by DP due to weaker metal-support interactions and a tendency for leaching over several cycles.

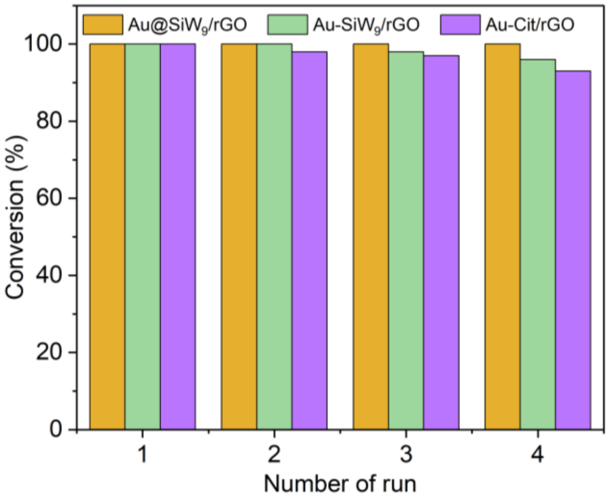

Figure 13: Catalytic stability test for the rGO-based catalysts.

Although the selective α, β-dehydrogenation of β-N-substituted saturated ketones is a reaction of considerable importance in both chemistry and medicine, there are only a few reports in the literature that explore the catalytic activity of supported metal nanoparticles for this type of transformation particularly for the oxidative dehydrogenation of 1-methyl-4-piperidone to 1-methyl-2,3-dihydropyridin-4(1H)-one. A summary of the current studies on this reaction using supported metal nanoparticles is given in Table 4. Notably, the highest conversion and yield have been achieved with the novel AuNP/rGO catalysts synthesized in this work.

Table 4: Comparison of catalytic studies on the oxidative dehydrogenation of 1-methyl-4-piperidone to 1-methyl-2,3-dihydropyridin-4(1H)-one with metal nanoparticles.

Catalysts	Solvent	Conversion (%)	Yield (%)	Ref.
Au-POM/AC	Water	92	86	[13]
Au/OMS-2	Water	94	90	[40]
Pd/Au/CeO2	Dimethylacetamide	/	79	[41]
$Pd(DMSO)_2(TFA)_2$	Ethyl acetate	/	74	[42]
Au-SiW_9/rGO	Water	100	98	This work
Au-Cit/rGO	Water	100	98	This work
Au@SiW_9/rGO	Water	100	97	This work
Au-Cit/AC	Water	100	91	This work

Conclusion

This study aimed to investigate the impact of carbon support nature, synthesis method, and coating ligand on the catalytic activity of gold nanoparticles. The findings highlight that the morphological and textural properties of the carbon support —here activated carbon (AC), carbon black (CB), and reduced graphene oxide (rGO) — play crucial roles in stabilizing nanoparticles and enhancing catalytic performance.

Among the supports, CB offers good nanoparticle dispersion but has limited functionalization capabilities and a low specific surface area. AC, on the other hand, provides a high surface area and functional groups that enhance metal-support interactions. However, both AC and CB suffer from mass transport limitations due to microporosity, which is a critical drawback in organic catalysis. In contrast, rGO emerges as the most effective support due to its large mesopore volume, which facilitates reactant diffusion and enhances catalytic efficiency.

The significant effect of polyoxometallate (POM SiW_9) is also emphasized, as it strongly stabilizes AuNPs This property helps maintain high catalytic activity over time, outperforming sodium citrate (NaCit) as a stabilizing ligand.

Regarding the synthesis methods, Deposition-Precipitation (DP) is generally more favourable for catalysis due to its ability to provide strong nanoparticle support and high stability under reaction conditions. However, it suffers from aggregation issues caused by uneven nucleation and support heterogeneity. Achieving a homogeneous dispersion of smaller nanoparticles remains a challenge, which is crucial for optimizing the catalytic surface area. In this regard, the Reduction-Precipitation (RP) method emerges as the more suitable synthesis approach, balancing nanoparticle size, dispersion, and catalytic efficiency.

In this study, we developed new effective and stable AuNP/carbon composite catalysts for the oxidative dehydrogenation (ODH) of 1-methyl-4-piperidone. Notably, reduced graphene oxide, which has been largely overlooked as a support catalyst in organic synthesis compared to activated carbon, demonstrated the best catalytic performance. These rGO-based AuNP catalysts are easy to synthesize and have achieved the highest yields reported in the literature to date. Hence, this finding offers novel approaches for developing metal nanoparticles on rGO-based supports for enhanced heterogeneous catalysis performance, identifying the mesoporosity as a key factor influencing activity. Importantly, this composite requires only a low loading of gold, can also use citrate as an inexpensive capping agent, making it a cost-effective and scalable option for broader market availability of the 1-methyl-2,3-dihydropyridin-4(1H)-one product. In follow-up work we will check if the AuNP/rGO composite can be applied to the general α, β-dehydrogenation of β-N-substituted saturated ketones.

Experimental

Catalyst's preparation

All chemicals used in this study were of analytical grade and were used as received without further purification: Acetone (≥99%, Sigma-Aldrich), potassium tetrachloridoaurate(III) (≥99%, BLD PHARMATECH GmbH), sodium citrate dihydrate (≥99%, VWR Chemicals), sodium borohydride (≥96.0%, Merck KGaA), 1-methyl-4-piperidone (≥99%, BLD PHARMATECH GmbH), sodium metasilicate nonahydrate (≥98%, Sigma-Aldrich), sodium tungstate (≥98%, Sigma-Aldrich), hydrochloric acid (37%, for analysis EMPARTA® ACS, Merck), activated charcoal, DARCO®, −100 mesh particle form, nanostructured powder (Cabot Corporation) and sodium carbonate anhydrous (≥99.5%, Sigma-Aldrich).

Reduced graphene oxide (rGO) was synthesized through a two-step process involving oxidation followed by thermal reduction, starting from natural graphite (type KFL 99.5, supplied by AMG Mining AG, formerly Kropfmühl AG, Passau, Germany). The oxidation step was carried out using the method developed by Hummers and Offeman [43], and the thermal reduction was performed at 750 °C [44].

Preparation of Au-Cit/AC, Au-Cit/rGO, and Au-Cit/CB by RD method

In a 500 mL Erlenmeyer flask 20 mg (53 µmol) $KAuCl_4$ were dissolved in 200 mL of water and brought to its boiling point at 100 °C on a magnetic stirring plate with a heating function while stirring continuously at 350 rpm. Once the solution reached the boiling point, 93 mg (319 µmol) of NaCit was added, causing the initially yellow solution to immediately become colorless, violet, and bright ruby red, indicating the formation of AuNPs [45]. The different carbon (AC: 1000 mg, rGO: 100 mg, CB: 500 mg) was then rapidly added (each in different batches of colloidal AuNPs) under vigorous stirring for another 15 minutes to ensure the complete deposition of AuNPs on the different carbon supports. The resulting suspension was then cooled to room temperature, filtered and thoroughly washed several times with deionized water to remove the excess of sodium citrate. The retained solids were dried in a vacuum oven at 60 °C for 24 hours, and stored in a sealed glass for further utilisations.

Preparation of Au-SiW_9/AC, Au-SiW_9/rGO, and Au-SiW_9/CB by RD method

The synthesis of colloidal AuNPs coated with SiW_9 was based on a method reported by Xia et al.[1] In a typical procedure, 50 mg of SiW_9 was dissolved in 55 mL of water and placed in an ice bath (~1 °C) to prevent isomerization of the polyoxometalate (POM). A 0.1 mol/L aqueous solution of $KAuCl_4$ (prepared by dissolving 5.7 mg of $KAuCl_4$ in 150 µL of water) was then added to the SiW_9 solution under stirring and allowed to react for 60 minutes. Subsequently, an ice-cold 0.03 mol/L $NaBH_4$ solution (5.6 mg of $NaBH_4$ dissolved in 5 mL of water) was added dropwise under continuous stirring. Upon complete addition of $NaBH_4$, the solution turned brown-orange, indicating the successful formation of AuNPs. Immediately after the $NaBH_4$ addition, different carbon supports (AC: 700 mg, rGO: 70 mg, CB: 350 mg) were separately introduced into different batches of the colloidal AuNPs solution under vigorous stirring. The mixtures were stirred for an additional 30 minutes to ensure the complete deposition of AuNPs onto the carbon supports. The resulting suspensions were then filtered and thoroughly washed with deionized water to remove excess SiW_9. The retained solids were dried in a vacuum oven at 60 °C for 24 hours and stored in sealed glass containers for further use.

Preparation of Au@SiW_9/AC, Au@SiW_9/rGO and Au@SiW_9/CB by DP method

This synthesis followed the same protocol as described above using the RD method with SiW_9, with the only difference being the order of reagent addition. After mixing the polyoxometalate (SiW_9) and the gold precursor solution under the same conditions for 60 minutes, different carbon supports (AC: 700 mg, rGO: 70 mg, CB: 350 mg) were separately introduced into different batches of the mixture. The stirring was continued for an additional 60 minutes before the dropwise addition of $NaBH_4$ under continuous stirring in each batch. After the reaction, the resulting suspension was cooled to room temperature, filtered, and thoroughly washed several times with deionized water to remove excess sodium citrate. The retained solids were then dried in a vacuum oven at 60 °C for 24 hours and stored for further use.

Catalytic procedure for the oxidation of 1-methyl-4-piperidone

A total of 0.25 mmol of 1-methyl-4-piperidone was dissolved in 2 mL of deionized water along with a specific amount of catalyst, which varied depending on the carbon support used in each reaction (see SI for details). The reaction was conducted in a glass tube under open-air conditions at 60 °C with vigorous stirring for 8 hours. Upon completion, the reaction mixture was separated from the catalyst by filtration using filter paper. The catalyst was then washed multiple times with a precise volume of acetone. The collected filtrate was analyzed directly by gas chromatography.

Recycling runs: The reusability of the catalysts was evaluated under optimized reaction conditions over four consecutive cycles, as shown in Figure 13. After each run, the catalyst was recovered from the reaction mixture by simple filtration using filter paper. The recovered catalyst was then thoroughly washed with acetone (4 × 30 mL) and water (3 × 30 mL) to remove any adsorbed reactants or products, followed by drying in an oven at 60 °C for 24h. The dried catalyst was subsequently reused in the next cycle under identical conditions without any additional catalyst being added.

Instrumental details

Gas Chromatography (GC) analyses were carried out using a Shimadzu GC-2014 with an autoinjector AOC-20i equipped with an FID-2014 detector, FS-Supreme-5ms 25 mm 0,25 × mm × 0,25 µm column and HS-10 headspace sampler. Gas Chromatography-Mass Spectrometry (GC-MS) spectra were performed using an Agilent technologies GC system equipped with an FID detector (7820A model), an auto-sampler (7693 model), and a mass selective detector (MSD 5977E model), HP-5MS 30 m × 0,25 mm ID × 0,25 µm Column. Proton Nuclear Magnetic Resonance (^{1}H-NMR) was performed using a Bruker 300 MHz spectrometer. Scanning Electron

Microscopy (SEM) were performed using a Jeol JSM-6510LV QSEM advanced electron microscope, operating at 20 kV with a LaB_6 cathode. The instrument was equipped with a Bruker Xflash 410 silicon drift detector, enabling energy-dispersive X-ray (EDX) spectrometric analysis to determine the elemental composition of the materials. UV–Vis Spectroscopy Spectral data were acquired using a VWR® UV/Visible Spectrophotometer P9, covering wavelengths from 250 nm to 1100 nm. Dynamic Light Scattering (DLS) was carried out using a Malvern Nano S Zetasizer equipped with a helium-neon (HeNe) laser operating at 633 nm. Transmission Electron Microscopy (TEM) was performed using a JEOL JEM-2100Plus electron microscope operating at 200 kV, coupled with a Matataki Flash camera. With the Gatan Digital Micrograph software (version 3.61), the size of over 200 particles was determined for the average diameter and the size distribution. The Powder X-ray Diffraction was recorded using the Rigaku MiniFlex600 (600 W, 40 kV, 15 mA). The measurements were carried out at RT using Cu Kα radiation (1.54182 Å). N2 adsorption experiments were done on the BELSorp-max II (MicrotracBEL Corporation).

Supporting Information

Additional experiment details, BET measurements, Powder X-ray diffraction (PXRD) measurement, TEM analysis, Carbon supports images, Gas Chromatography (GC), Gas Chromatography-Mass Spectrometry (GC-MS), ^{1}H-NMR spectroscopy, Gold loading, Turnover number and turnover frequency.

Acknowledgements

We thank the Core Facility for Electron Microscopy of the Institute of Medical Faculty of the Heinrich Heine University Düsseldorf for access to the JEOL JEM-2100Plus electron microscope instrument.

We thank the Center for Molecular and Structural Analytics at Heinrich Heine University Düsseldorf (CeMSA@HHU) for NMR measurements.

We sincerely thank Dr. Dimitrios Tzalis, CEO of Taros Chemicals GmbH & Co. KG, for providing access to the GC-MS instrumentation.

We are deeply grateful to Dr. István Boldog for his insightful advice, continuous support, and valuable scientific contributions to this work.

Funding

German Academic Exchange Service (DAAD) under grant no. 57645448.

References

1. Adil, S. F.; Ashraf, M.; Khan, M.; Assal, M. E.; Shaik, M. R.; Kuniyil, M.; Al-Warthan, A.; Siddiqui, M. R. H.; Tremel, W.; Tahir, M. N. *Chem. Rec.*, **2022**, *22*, 1527-8999. doi.org/10.1002/tcr.202100274.
2. Chadha, U.; Selvaraj, S. K.; Ashokan, H.; Hariharan, S. P.; Paul, V. M.; Venkatarangan, V.; Paramasivam, V. *Adv. Mater. Sci. Eng.*, **2022**, *2022*, 1687-8434. doi.org/10.1155/2022/1552334.
3. Irshad, A. W.; Sapan, K. J.; Huma, K.; Abul, K.; Tokeer, A. *Curr. Pharm. Biotechnol.*, **2021**, 22, 724-732. doi.org/10.2174/1389201022666210218195205.

4. Bano, A.; Dawood, A.; Rida, F.; Saira, F.; Malik, A.; Alkholief, M.; Ahmad, H.; Khan, M. A.; Ahmad, Z.; Bazighifan, *O. Sci. Rep.*, **2023**, 13, 12359. doi.org/10.1038/s41598-023-38234-2.

5. Narayanan, R.; El-Sayed, M. A. *J. Phys. Chem. B*., **2004**, 108, 5726-5733. doi.org/10.1021/jp0493780.

6. Alshammari, A. S., *Catalysts*, **2019**, *9*, 402**.** doi.org/10.3390/catal9050402.

7. Liu, B.; Yao, H.; Song, W.; Jin, L.; Mosa, I. M.; Rusling, J. F.; Suib, S. L.; He, J. *J. Am. Chem. Soc.*, **2016**, *138*, 4718-4721. doi.org/10.1021/jacs.6b01702.

8. Zhang, M.; Hao, J.; Neyman, A.; Wang, Y.; Weinstock, I. A. *Inorg. Chem.*, **2017**, 56, 2400–2408. doi:10.1021/acs.inorgchem.6b02167.

9. Weinstock, I. A.; Schreiber, R. E.; Neumann, R. *Chem. Rev.,* **2018**, *118*, 2680–2717. doi:10.1021/acs.chemrev.7b00444.

10. Wang, S. S.; Yang, G. Y. *Chem. Rev.*, **2015**, *115*, 4893–4962. doi:10.1021/cr500390v.

11. Martín, S.; Takashima, Y.; Lin, C.-G.; Song, Y.-F.; Miras, H. N.; Cronin, L. *Inorg. Chem.*, **2019**, *58*, 4110–4116. doi:10.1021/acs.inorgchem.8b03013.

12. Keita, B.; Liu, T.; Nadjo, L. *J. Mater. Chem.* **2009**, *19*, 19–33. doi:10.1039/B813303D.

13. Xia, K.; Yatabe, T.; Yonesato, K.; Yabe, T.; Kikkawa, S.; Yamazoe, S.; Nakata, A.; Yamaguchi, K.; Suzuki, K. *Angew. Chem. Int. Ed.* **2022**, *61*, e202205873. doi:10.1002/anie.202205873.

14. Cetin, A.; Ilk Capar, M. *J. Phys. Chem. B*, **2022**, *126*, 5534–5543. doi:10.1021/acs.jpcb.2c01132.

15. Huang, R.; Fedeli, S.; Hirschbiegel, C.-M.; Zhang, X.; Rotello, V. M. *ACS Nanosci. Au,* **2024**, *4*, 62–68. doi:10.1021/acsnanoscienceau.3c00042.

16. Masoud, N.; Partsch, T.; de Jong, K. P.; de Jongh, P. E. *Gold Bull.,* **2019**, *52*, 105–114. doi:10.1007/s13404-019-00259-9.

17. Pereira, M. F. R.; Órfão, J. J. M.; Figueiredo, J. L. *Appl. Catal. A Gen.*, **2001**, *218*, 307–318. doi:10.1016/S0926-860X(01)00657-3.

18. Rodríguez-Reinoso, F. *Carbon,* **1998**, *36*, 159–175. doi:10.1016/S0008-6223(97)00173-5.

19. Figueiredo, J. L.; Pereira, M. F. R. *Catal. Today,* **2010**, *150*, 2–7.

20. Corma, A.; Garcia, H. *Chem. Soc. Rev.,* **2008**, *37*, 2096–2126. doi:10.1039/B707314N.

21. Grunewald,G. C.; Drago, R. S. *J. Mol. Catal.*, **1990**, *58*, 227–233. doi:10.1016/0304-5102(90)85042-G.

22. Seebacher, W.; Hoffelner, M.; Belaj, F.; Pirker, T.; Alajlani, M.; Bauer, R.; Pferschy Wenzig, E.-M.; Saf, R.; Weis, R. *Molecules,* **2023**, *28*, 6869. doi:10.3390/molecules28196869.

23. Thommes, M.; Kaneko, K.; Neimark, A. V.; Olivier, J. P.; Rodriguez-Reinoso, F.; Rouquerol, J.; Sing, K. S. W. *Pure Appl. Chem.,* **2015**, *87*, 1051–1069. doi:10.1515/pac-2014-1117.

24. Rodrigues, E. G.; Pereira, M. F. R.; Chen, X.; Delgado, J. J.; Órfão, J. J. M. *J. Catal.,* **2011**, *281*, 119–127. doi:10.1016/j.apcatb.2011.12.008.

25. Rodrigues, E. G.; Delgado, J. J.; Chen, X.; Pereira, M. F. R.; Órfão, J. J. M. *Ind. Eng. Chem. Res.,* **2012**, *51*, 15884–15894. doi:10.1021/ie302159m.

26. Zhu, J.; Carabineiro, S. A. C.; Shan, D.; Faria, J. L.; Zhu, Y.; Figueiredo, J. L. *J. Catal.*, **2010**, *274*, 207–214. doi:10.1016/j.jcat.2010.06.018.

27. Yu, X.; Huo, Y.; Yang, J.; Chang, S.; Ma, Y.; Huang, W. *Appl. Surf. Sci.,* **2013**, *280*, 450–455. doi:10.1016/j.apsusc.2013.05.008.

28. Studebaker, M. L.; Huffman, E. W. D.; Wolfe, A. C.; Nabors, L. G. *Ind. Eng. Chem.,* **1956**, *48*, 162–166.

29. Tézé, A.; Hervé, G.; Finke, R. G.; Lyon, D. K. *Inorg. Synth.*, **1990**, *27*, 85－96. doi:10.1002/9780470132586.

30. Carabineiro, S. A. C., *Front. Chem.*, **2019**, *7*, 702. doi:10.3389/fchem.2019.00702.

31. Mohammad, A. M.; Abdelrahman, A. I.; El-Deab, M. S.; Okajima, T.; Ohsaka, T. *Colloids Surf. A*, **2008**, *318*, 78–83. doi:10.1016/j.colsurfa.2007.12.013.

32. Stetsenko, M.; Margitych, T.; Kryvyi, S.; Maksimenko, L.; Hassan, A.; Filonenko, S.; Li, B.; Qu, J.; Scheer, E.; Snegir, S. *Nanomaterials,* **2020**, *10*. 512. doi:10.3390/nano10030512.

33. Sneha, K.; Sathishkumar, M.; Kim, S.; Yun, Y.-S. *Process Biochem.,* **2010**, *45*, 1450–1458. doi:10.1016/j.procbio.2010.05.019.

34. Chen, D.; Li, L.; Guo, L. *Nanotechnology,* **2011**, *22*, 325601. doi:10.1088/0957-4484/22/32/325601.

35. Ingham, B.; Toney, M. F. In *Metallic Films for Electronic, Optical and Magnetic Applications*; Barmak, K., Coffey, K., *Eds.; Woodhead Publishing* **2014**, 3–38. doi:10.1533/9780857096296.1.3.

36. Oliveira, A. E. F.; Pereira, A. C.; Resende, M. A. C.; Ferreira, L. F. *Analytica,* **2023**, *4*, 250–263. doi:10.3390/analytica4020020.

37. Miranda, M. A. R.; Sasaki, J. M. *Acta Crystallogr., Sect. A: Found. Adv.* **2018**, *74*, 54–65. doi:10.1107/S2053273317014929.

38. Rabiei, M.; Palevicius, A.; Monshi, A.; Nasiri, S.; Vilkauskas, A.; Janusas, G. *Nanomaterials*, **2020**, *10*, 1627. doi:10.3390/nano10091627.

39. Zhang, H.; Hines, D.; Akins, D. L., *Dalton Trans.*, **2014**, *43*, 2670–2675. doi:10.1039/C3DT52573B.

40. Yoshii, D.; Jin, X.; Yatabe, T.; Hasegawa, J.-Y.; Yamaguchi, K.; Mizuno, N. *Chem. Commun.*, **2016**, *52*, 14314–14317. doi:10.1039/C6CC07846J.

41. Takei, D.; Yatabe, T.; Jin, X.; Yabe, T.; Mizuno, N.; Yamaguchi, K. *ACS Catal.*, **2020**, *10*, 5057–5063. doi:10.1021/acscatal.0c00277.

42. Diao, T.; White, P.; Guzei, I.; Stahl, S. S. *Inorg. Chem.* **2012**, *51*, 11898–11909. doi:10.1021/ic301799p.

43. Hummers, W. S., Jr.; Offeman, R. E. *J. Am. Chem. Soc.,* **1958**, *80*, 1339. doi:10.1021/ja01539a017.

44. Schmitz, A.; Schütte, K.; Ilievski, V.; Barthel, J.; Burk, L.; Mülhaupt, R.; Yue, J.; Smarsly, B.; Janiak, C. *Beilstein J. Nanotechnol.* **2017**, *8*, 2474–2483. doi:10.3762/bjnano.8.247.

45. Giesen, B.; Nickel, A.-C.; Barthel, J.; Kahlert, U. D.; Janiak, C. *Pharmaceutics* **2021**, *13*, 295. doi:10.3390/pharmaceutics13020295.